Origin of the Boosting Effect of Polyoxometalates in Photocatalysis: The Case of CO 2 Reduction by a Rh-Containing Metal–Organic Framework

Albert Solé-Daura, Youven Benseghir, Minh-Huong Ha-Thi, Marc Fontecave, Pierre Mialane, Anne Dolbecq, Caroline Mellot-Draznieks

Origin of the Boosting Effect of Polyoxometalates in Photocatalysis: the case of CO_2 Reduction by a Rh-Containing Metal-Organic Framework.

Albert Solé-Daura,[⊥,†,*] Youven Benseghir,[⊥,§] Minh-Huong Ha-Thi,[‡] Marc Fontecave,[⊥] Pierre Mialane,[§] Anne Dolbecq[§] and Caroline Mellot-Draznieks[⊥,*]

[⊥] Laboratoire de Chimie des Processus Biologiques, UMR CNRS 8229, Collège de France, Université Pierre et Marie Curie, PSL Research University, 11 Place Marcelin Berthelot, 75231 Paris Cedex 05, France.

[§] Université Paris-Saclay, UVSQ, CNRS, Institut Lavoisier de Versailles, 78000 Versailles, France.

[‡] Université Paris-Saclay, CNRS, Institut des Sciences Moléculaires d'Orsay, 91405 Orsay, France.

KEYWORDS: DFT, Metal-Organic Frameworks, Polyoxometalates, CO_2 photoreduction, Hydrogen Evolution.

ABSTRACT: The immobilization of polyoxometalates (POMs) near catalytic centers of Metal-Organic Frameworks (MOFs) has been reported as an advantageous strategy to boost their photocatalytic activity towards strategic reactions such as CO_2 reduction (CO_2RR) or hydrogen evolution (HER), although the reasons for such enhancement are still poorly understood. Unveiling the role of POM guests in the reaction mechanisms is therefore a key step towards the development of the next generation of multi-component catalytic materials with optimal photocatalytic performances. Here, we elucidate the remarkable role of encapsulated $[PW_{12}O_{40}]^{3-}$ (**PW_{12}**) polyoxometalates in boosting the photocatalytic activity of the Rh-functionalized UiO-67 MOF towards CO_2RR and HER by combining theoretical DFT and microkinetic modelling approaches with experimental photophysical and spectroscopic techniques. Firstly, we characterized a new detailed mechanism for CO_2RR and HER catalyzed by the **PW_{12}**-containing Rh-functionalized MOF, using $[Ru(bpy)_3]^{2+}$ as the photosensitizer (PS) and triethanolamine (TEOA) as sacrificial electron donor in acetonitrile. Our results reveal that the encapsulated POMs act as efficient electron reservoirs, which quench $[Ru(bpy)_3]^{+}$ - the photogenerated reduced form of the PS - and transfer the electrons to the Rh catalytic sites of the MOF. Notably, this is shown to favor the regeneration of the oxidized PS over its unproductive degradation, boosting the turnover numbers of the photocatalytic system. Such mechanism can explain not only the higher formate and H_2 product yields in the POM-containing catalyst, but also the experimentally observed higher impact on the HER pathway than that on the CO_2RR one, as the source of protons is generated in the reductive quenching of the photoexcited PS by TEOA. Finally, our computational exploration was extended to a whole variety of POMs, which allowed establishing relationships between their redox potentials and the activity of the related **POM**-containing catalytic materials. The optimal activity is reached when both the ability of the POM to accept electrons and that of its reduced form to reduce the Rh catalyst are simultaneously maximized, leading to a volcano plot whereby POMs with moderate redox potential display the highest impact on photocatalytic performances.

INTRODUCTION

The reduction of CO_2 (CO_2RR) is an attractive approach to simultaneously tackle two important societal challenges, that are the urgent need for reducing the atmospheric CO_2 emissions and the synthesis of value-added products, including fuels and commodity chemicals, using a cheap and readily available carbon feedstock.[1,2] Using solar light as a renewable energy source to promote photocatalytic CO_2RR is also a highly pursued goal within the context of the current transition to a greener and fossil fuel-independent society.[3,4] In this regard, the development of photocatalytic platforms for CO_2RR represents an ever-growing research field, whereby many efforts have been devoted to improve their activity and in turn, their quantum efficiency.

Polyoxometalates (POMs) are polynuclear, anionic, metal oxide clusters usually composed by early transition-metal atoms in their highest oxidation state, such as W(VI), Mo(VI) or V(V).[5,6] Owing to the high oxidation state of metal centers in POMs, their lowest set of unoccupied molecular orbitals consists of linear combinations of d-type orbitals from the metals with strong leaning towards accepting electrons,[7] which allow them to be reversibly reduced multiple times within relatively narrow potential ranges.[8-11] Taking advantage of these properties, but also of their high thermal stability and high tunability, POMs have been successfully used to boost or to enable the photo- and electrocatalytic activity of both homogeneous and heterogeneous catalysts, including examples of strategic reactions such as CO_2RR and hydrogen evolution (HER).[12-25] Typically, in an early example of {Re(L)-POM} hybrid complex,[12,13] the non-covalent attachment of the non-catalytic POM to the (Re)bpy(CO)$_3$ CO_2-to-CO reduction catalyst has been shown to allow efficient charge transfer from the reduced POM to the Re catalyst under illumination, the POM acting as a photosensitizer (PS), electron reservoir and electron donor. More recently, it was reported that the electron-transfer property of the POM@PCN-222(Co) composite occurring in the electrocatalytic conversion of CO_2 into CO was enhanced owing to the directional electron-transfer from the mixed-valence POM to Co single-metal sites of the porphyrinic MOF.[18] Still, although such boosting effect occurring in homogeneous or heterogeneous conditions is commonly ascribed to the possible roles of POMs as electron or proton relays, the origin of the beneficial interplay between POMs and catalytic sites often remains to be

elucidated, and more generally still misses rationale, thus hindering the development of clear design strategies.

Very recently, the immobilization of a Keggin-type POM anion, namely $[PW_{12}O_{40}]^{3-}$ or **PW_{12}** for short, inside the octahedral pores of a Rh-functionalized UiO-67 catalyst was shown to provide a significant enhancement of its photocatalytic activity towards CO_2RR and HER.[26] The Rh-based $[(Cp^*)Rh(bpydc)Cl]^+$ ($Cp^* = \eta^5$-$C_5(CH_3)_5$; bpydc = 2,2'-bipyridine-5,5'-dicarboxylic acid) molecular catalyst,[27] namely RhCp*, was originally immobilized within the Zr-based UiO-67 MOF by linker exchange, leading to the RhCp*@UiO-67 catalytic material.[28] This strategy allowed overcoming the recyclability issues underlying homogeneous catalysts, while improving the stability of the Rh-catalyst in the RhCp*@UiO-67 by preventing its deactivation via dimerization. In both homogeneous and heterogeneous conditions, RhCp* was found to produce $HCOO^-$ under visible-light irradiation from CO_2-saturated acetonitrile solutions using $[Ru(bpy)_3]^{2+}$ as PS and triethanolamine (TEOA) as sacrificial electron and proton donor, along with H_2 depending on the used porous host.[28-30]

In a more ambitious goal, both the RhCp* catalyst and the **PW_{12}** POM were successfully co-immobilized within the framework of the UiO-67, leading to the (**PW_{12}**,RhCp*)@UiO-67 material (Figure 1a). With the latter, the yield of $HCOO^-$ and H_2 was found to be respectively ca. 2 and 2.5 times higher than that in the POM-free system (see Figure 1b and Table S1) under the same photocatalytic conditions (visible light irradiation, $\lambda \geq 415$ nm, in 5:1 (v/v) CH_3CN:TEOA solutions containing $[Ru(bpy)_3]^{2+}$ as PS).[26] An in-depth structural characterization of the (**PW_{12}**,RhCp*)@UiO-67 catalyst confirmed the integrity of the POM once encapsulated in UiO-67 and revealed that POMs are preferably located in the vicinity of RhCp* catalytic site inside the material as shown in Figure 1a. However, their participation in the reaction mechanism, as well as the origin of the enhanced photocatalytic performance both remain to be elucidated. More generally, these recent detailed findings not only offer a unique opportunity to elucidate the beneficial role of **PW_{12}** in the photocatalytic performances of (**PW_{12}**,RhCp*)@UiO-67 but also open new questions regarding how such beneficial guest species should be selected in order to target specific enhanced performances and selectivities for CO_2RR and HER.

Herein, we carried out a comprehensive theoretical study by means of DFT calculations and microkinetic modelling techniques to investigate the role of encapsulated POMs in boosting the photocatalytic activity in the (**PW_{12}**,RhCp*)@UiO-67 material. To do so, we initially analyzed in detail the mechanisms underlying the photocatalytic activity of the POM-free system, which were then compared to those prevailing in (**PW_{12}**,RhCp*)@UiO-67. This theoretical analysis is complemented by experimental photophysical and spectroscopic analyses, which aided the identification of the redox states accessible to the photosensitizer in solution and supported the conclusions derived from the theoretical work. Finally, we performed a systematic investigation of the potential impact of a wide variety of POMs differing in their overall charge, structure and composition on the CO_2RR and HER performances of {POM,RhCp*} combinations. The latter allowed setting structure-activity relationships via the construction of a volcano plot that relates the redox potential of the POM with the activity of the derived (POM,RhCp*)@UiO-67 catalytic material.

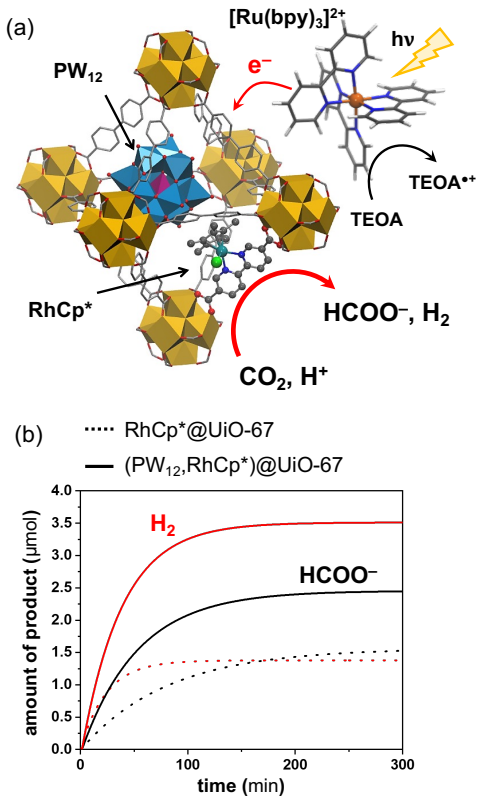

Figure 1. (a) Representation of an octahedral pore of the (**PW_{12}**,RhCp*)@UiO-67 catalyst for the photoreduction of CO_2 and H^+ in the presence of $[Ru(bpy)_3]^{2+}$ and TEOA. The {RhCp*(bpydc)Cl} linker is highlighted with ball-and-sticks; red spheres: O, dark grey spheres: C, blue spheres: N, green sphere: Cl, dark green sphere: Rh. The POM and MOF nodes are represented with polyhedra (blue: WO_6; pink: PO_4; orange: ZrO_8). Hydrogen atoms are omitted for clarity. (b) Comparison of the experimental evolution with time of $HCOO^-$ and H_2 products using RhCp*@UiO-67 (dotted lines) and (**PW_{12}**,RhCp*)@UiO-67 (solid lines) as catalysts. Data reconstructed from ref. 26.

RESULTS AND DISCUSSION

In light of the experimental and computational investigations reported so far in homogeneous conditions on the RhCp* system,[27,29,31,32] we propose the catalytic cycle depicted in Figure 2 for the RhCp*@UiO-67 system. In the first step, the two-electron reduction of the Rh(III) center triggers the decoordination of the chloride ligand to give a Rh(I) species, which is then protonated by a proton source to generate a Rh(III)-hydride. As evidenced by electrochemical studies,[27,31,32] the latter needs to undergo a third reduction occurring on the bipyridine (bpy) group of the ligand (highlighted in red in Figure 2) in order to generate the active radical form of the catalyst. The latter is then hydridic enough to transfer a hydride to an incoming electrophile such as CO_2 or H^+ to yield the $HCOO^-$ and H_2 products, respectively. Finally, a one-electron reduction of the catalyst regenerates the Rh(I) species, closing the catalytic cycle.

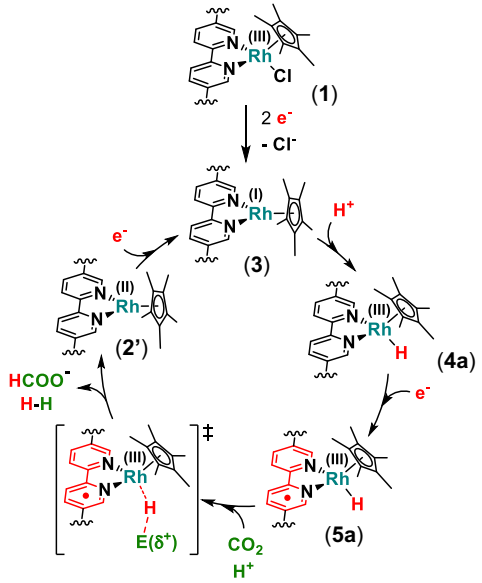

Figure 2. Proposed mechanism for the catalytic reduction of CO_2 and H^+ into $HCOO^-$ and H_2, respectively, by the RhCp* catalyst. E(δ⁺) stands for an electrophilic center of the substrate (C atom in CO_2 or H^+). Labels in parentheses correspond to those assigned throughout the mechanistic exploration (vide infra).

1. Photoinduced generation of electron and proton donors. As the formation of the active form of the catalyst requires several reduction and protonation steps, we initially identified the nature of the possible electron and proton sources that may be generated under photocatalytic conditions.

The ground state of the PS is known to generate metal-to-ligand charge transfer (MLCT) singlet excited states under visible-light irradiation, which rapidly undergoes intersystem crossing and relaxes to the most stable and long-lived (up to 1100 ns in CH_3CN)[33] MLCT triplet, $^3[Ru^{III}(bpy)_2(bpy^{\bullet-})]^{2+,*}$.[34] This ^{3}MLCT state, labeled as $[Ru(bpy)_3]^{2+,*}$ for simplicity, can be seen as a potential electron donor species (with a E^o_{red} of -0.56 V vs NHE for the $[Ru^{III}(bpy)_3]^{3+} + e^- \rightarrow {}^3[Ru^{III}(bpy)_2(bpy^{\bullet-})]^{2+,*}$ half reaction).[35,36] Alternatively, $[Ru(bpy)_3]^{2+,*}$ can be also reductively quenched by an electron donor, here TEOA, to form the one-electron reduced $[Ru(bpy)_3]^+$ complex in addition to a $TEOA^{\bullet+}$ molecule (Figure S1). The latter displays a much stronger reductive power (E^o_{red} of -1.08 V vs NHE) than $[Ru(bpy)_3]^{2+,*}$ (-0.56 V). Still, the ability of TEOA to promote the reductive quenching of $[Ru(bpy)_3]^{2+,*}$ has been a matter of debate in the literature. While several studies showed no significant variations of the $[Ru(bpy)_3]^{2+,*}$ lifetimes in the presence of TEOA,[37-39] some other authors proposed such a process as required to obtain a reducing agent strong enough to explain the observed reduction of other species, such as catalysts or substrates.[40-45] Although our DFT calculations suggest that such a reductive quenching is thermodynamically favorable in high concentrations of TEOA, it is not possible to unambiguously determine whether it is kinetically accessible (see SI for details). For this reason, we next performed transient absorption spectroscopy (TAS) measurements of a 5:1 (v/v) CH_3CN/TEOA solution containing 26 μM $[Ru(bpy)_3]Cl_2$.

As shown in Figure 3a, the presence of TEOA causes a loss of ground state bleaching of $[Ru(bpy)_3]^{2+}$ at 460 nm in the transient absorption spectra, together with the appearance of a new absorption band centered at 510 nm. This is the clear signature of the formation of a $[Ru(bpy)_3]^+$ species,[46,47] which proves the ability of TEOA to reductively quench the $[Ru(bpy)_3]^{2+,*}$ species at the concentrations used in photocatalytic experiments. Additional photo-irradiation experiments (Figure 3b) showed the decrease of the $[Ru(bpy)_3]^{2+}$ absorption band at 450 nm initially accompanied by the appearance of the band at 510 nm of $[Ru(bpy)_3]^+$ which is followed by an increase of red absorption tail due to the degradation of the solution (see Figure S2 for differential absorption spectra). This degradation is related to the low stability of $[Ru(bpy)_3]^+$ over extended periods, most likely caused by the loss of a bpy ligand triggered by the population of metal-centered states,[34,48-50] and will be minimized with the presence of catalyst, which is in line with previous observations.[51] Thus, $[Ru(bpy)_3]^+$ can be formed under photocatalytic conditions and as such, it can be considered to act as the reducing species that reduces the catalyst.

Regarding the proton source, Fujita and coworkers recently showed that mixtures of TEOA and CO_2 are in equilibrium with a zwitterionic covalent alkylcarbonate (Scheme S1),[52] which was further proposed to play the role of a proton source.[53] Our calculations indicate that, indeed, this zwitterionic alkylcarbonate may act as a proton source, although protonation steps are more favorable with an N-protonated TEOA, namely $HTEOA^+$, which is generated after the reductive quenching of $[Ru(bpy)_3]^{2+,*}$ upon deprotonation of $TEOA^{\bullet+}$ (see Figure S1 and related text in the SI for further details).[54-57] Thus, $HTEOA^+$ is identified as the main source of protons in our system. One should also note that the deprotonation of $HTEOA^+$ by traces of water is rather unfavorable (ΔG = +27.2 kcal mol^{-1} considering a water dimer as proton acceptor to give a Zundel cation, $H_5O_2^+$, in acetonitrile). Therefore, free protons were not considered to participate in the reaction mechanism.

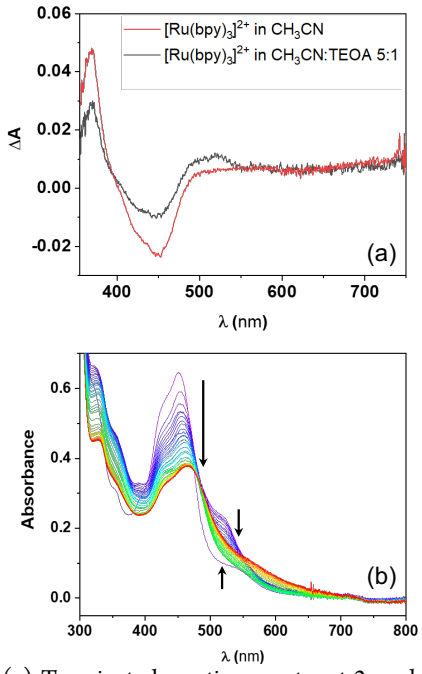

Figure 3. (a) Transient absorption spectra at 2 μs delay times of $[Ru(bpy)_3]^{2+}$ in degassed CH_3CN (red line) and in 5:1 CH_3CN:TEOA (black line) after excitation at 460 nm. (b) Evolution of the UV-Vis spectrum of $[Ru(bpy)_3]^{2+}$ (26 μM) in degassed 5:1 CH_3CN:TEOA during photo-irradiation from 0 (purple) to 2100 (red) seconds with LED at 456 nm.

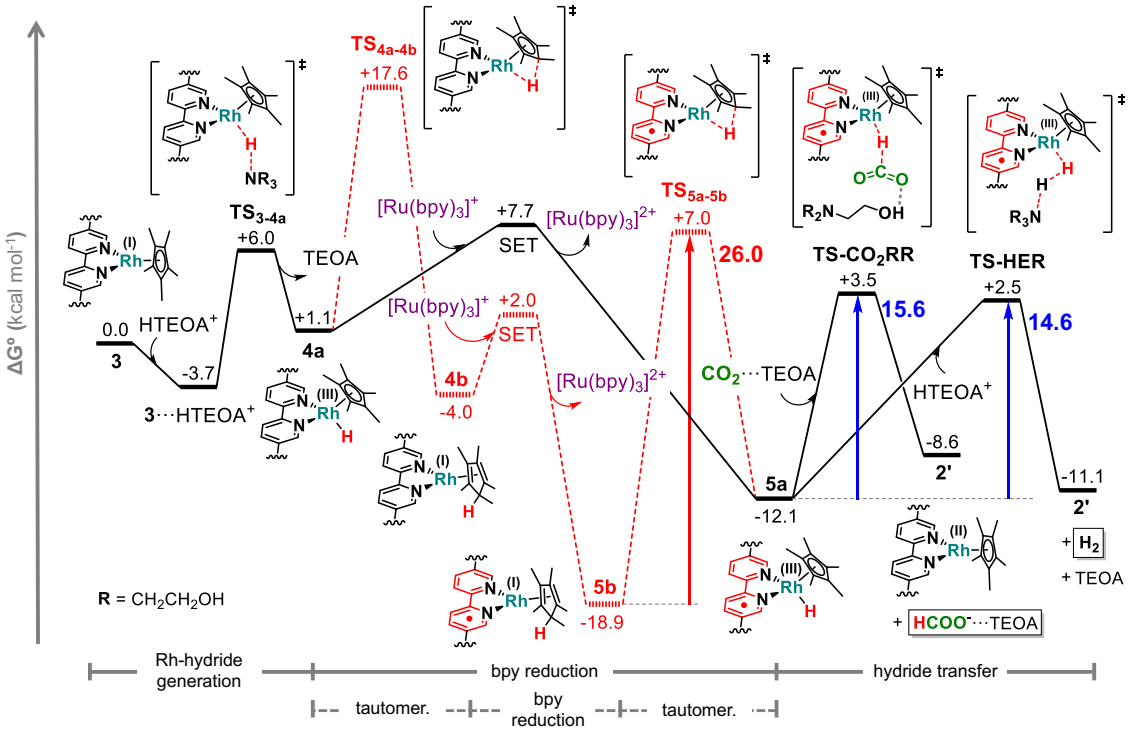

Figure 4. Gibbs free energy profile (kcal mol^{-1}) for the reduction of CO_2 into formate and H^+ into molecular hydrogen promoted by **3**. Dashed red lines denote an alternative higher energy pathway that prevails at low concentration of photosensitizer.

2. Reaction mechanism for the photo-reduction of CO_2 and protons catalyzed by RhCp*@UiO-67. With the gained knowledge about the nature of the proton and electron sources generated upon light irradiation, we next analyzed in detail the reaction mechanism governing the reactivity of the POM-free system by means of DFT calculations. These calculations were performed on a cluster model consisting of a Rh-containing linker of the MOF, whereby the terminal carboxylate groups were capped with H atoms (see Computational details section for further details). The initial reduction steps of the Rh(III)-chloride species (**1**) can be easily attained by $[Ru(bpy)_3]^+$ through two consecutive SET steps to generate, first, the Rh(II) species **2'** upon releasing the chloride ligand, and then, the Rh(I) intermediate **3** (see Scheme S2). Species **3** was found to exhibit a singlet ground state, although the lowest triplet state is only 0.5 kcal mol^{-1} less stable. Conversely, the reduction of **1** by $[Ru(bpy)_3]^{2+,*}$ involves free-energy barriers that are too high (ca. 13-14 kcal mol^{-1}, Scheme S2) to compete with the decay of $[Ru(bpy)_3]^{2+,*}$ to the ground state, which translates into a barrier of ca. 9 kcal mol^{-1} according to its experimental lifetime[33] and assuming first-order kinetics. Thus, $[Ru(bpy)_3]^{2+,*}$ is not a strong enough reductant to promote the efficient activation of the catalyst, indicating that the generation of stronger reducing species, i.e. $[Ru(bpy)_3]^+$, is required for the catalysis. Notably, this is further supported by additional TAS measurements, which showed negligible interaction between $[Ru(bpy)_3]^{2+,*}$ and the **RhCp*** catalyst (Figure S3). Radical species involved in the $TEOA^{\bullet+}$ degradation are also less likely than $[Ru(bpy)_3]^+$ to promote the reduction of **1** (Scheme S2). It is important to note that $[Ru(bpy)_3]^+$, with a diameter of approximately 13 Å, is too bulky to go into the pores of the UiO-67 MOF, which has a pore window size of ca. 8 Å. We thus assumed that SET processes between the reduced PS and the catalytic sites (and POM guests in (**PW_{12}**,RhCp*)@UiO-67; *vide infra*) take place at the surface of the MOF. Nonetheless, due to the presence of redox-active Rh-containing linkers, electrons can then diffuse to more inner regions of the MOF to grant catalytic activity to more hindered Rh centers.[58,59] Such electron diffusion is expected to be further eased in (**PW_{12}**,RhCp*)@UiO-67, since the electric conductivity of MOFs is known to be greatly enhanced upon the incorporation of redox-active guests such as POMs[60] or fullerenes.[61]

Figure 4 displays the Gibbs free-energy profile for the reduction of CO_2 and H^+ into formate and H_2, respectively, promoted by species **3**. Firstly, the protonation of **3** by $HTEOA^+$ proceeds through a smooth free-energy barrier of 9.7 kcal mol^{-1} (**$TS_{3\text{-}4a}$**) from the non-covalent **3**···$HTEOA^+$ adduct. This yields the Rh(III)-hydride species **4a**, which lies slightly above **3** in terms of free energy. The formation of metal hydrides assisted by amines has been proposed before for the RhCp* catalyst in homogeneous conditions,[29] but also for other catalysts in the context of CO_2RR.[62-64] Also of note, this process is faster than the putative coordination of CO_2 to **3**, which involves a higher, overall free-energy barrier of 14.8 kcal mol^{-1}, in line with the product selectivity towards formate. As shown in Figure 1b, the experimental evolution of the products concentration over time follows a logarithmic growth, reaching a plateau after ca. 90 min in the RhCp*@UiO-67 system.[26] This was ascribed to the degradation of the photosensitizer, since addition of fresh $[Ru(bpy)_3]^{2+}$ to the reaction mixture was found to resume the reaction with a rate comparable to the initial one.[26] Consequently, two regimes may be differentiated in the free-energy profile, depending on the concentration of $[Ru(bpy)_3]^+$ along the reaction. In the first regime (black line pathway in Figure 4), when the concentration of $[Ru(bpy)_3]^+$ is high enough, a rapid SET from $[Ru(bpy)_3]^+$ to **4a** can trigger the formation of **5a**, which is the active form of the catalyst. This step is exergonic by 13.2 kcal mol^{-1} and proceeds through a low free-energy barrier of 6.6 kcal mol^{-1}. Species **5a** can then transfer a nucleophilic

hydride to either the carbon atom of an incoming CO_2 molecule or to a N-bound proton of $HTEOA^+$ through outer-sphere mechanisms,[29] giving access to formate and H_2 products, respectively.

The reduction of CO_2 occurs through **TS-CO$_2$RR** involving a smooth free-energy barrier of 15.6 kcal mol^{-1} from **5a**. This process is assisted by a TEOA molecule interacting with the CO_2 fragment via hydrogen bonding, which stabilizes the increased negative charge supported by the CO_2 oxygens in the TS structure. Without the assistance of TEOA, the CO_2RR barrier increases by 2.2 kcal mol^{-1}. The interaction between CO_2 and TEOA does not only occur during the hydride-transfer process, but also in solution, being thermodynamically favorable by 2.3 kcal mol^{-1}. This thus suggests that CO_2 migrates together with a TEOA molecule to the catalytic sites. The as generated formate product is then released to the solution as a $HCOO^-$···TEOA non-covalent adduct (with an interaction free energy of -11.5 kcal mol^{-1}), while the electron in the bpy ligand of the catalyst migrates to the Rh center to regenerate species **2'**. Although the reduction of CO_2 to formate from **5a** is endergonic by 3.5 kcal mol^{-1}, the subsequent reduction of **2'** by $[Ru(bpy)_3]^+$ to regenerate species **3** renders the overall process exergonic and irreversible (see Scheme S2). The protonation of the $HCOO^-$···TEOA adduct by a $HTEOA^+$ molecule to give HCOOH···TEOA is predicted to be slightly exergonic (ΔG = -0.6 kcal mol^{-1}) and therefore, both the protonated and deprotonated forms of the product might coexist in the reaction mixture. One should also note that the coordination of formate to **2'** is endergonic by 2.4 kcal mol^{-1} and therefore, it is not expected to influence the overall kinetics of the reaction. On the other hand, the HER proceeds through **TS-HER**, in which the Rh-hydride is transferred to $HTEOA^+$, promoting the H—N^+ bond cleavage and releasing a TEOA molecule. This process readily generates H_2 overcoming a free-energy barrier of 14.6 kcal mol^{-1}, which is very similar to that obtained for the CO_2RR pathway (15.6 kcal mol^{-1}).

In a second regime (dashed line pathway in Figure 4), the concentration of $[Ru(bpy)_3]^+$ in solution is expected to be rather low after several hours of reaction due to the degradation process mentioned above. As a consequence, the formation of products through the black line pathway in Figure 4 would still be operative, although the proton-hydride tautomerization of **4a** into the more stable **4b**,[65-68] overcoming a free-energy barrier of 16.5 kcal mol^{-1}, might prevail over the direct reduction of **4a** into **5a** by $[Ru(bpy)_3]^+$. This tautomerization occurs through **TS$_{4a\text{-}4b}$**, whereby the Rh-hydride inserts into a Rh—C(Cp*) bond in **4a** reducing the Rh(III) ion into Rh(I). Akin to **4a**, **4b** can be easily reduced at the bpy ligand by $[Ru(bpy)_3]^+$, leading to species **5b** through a favorable SET step (Figure 4). The active form of the catalyst (**5a**) can be reached from **5b** through another intramolecular proton-hydride tautomerism, which can be seen as the reverse process to that described above. This step proceeds uphill (ΔG = +6.8 kcal mol^{-1}) and needs to overcome a rather high free-energy barrier of 26 kcal mol^{-1}, involving **TS$_{5a\text{-}5b}$**. As both **TS-CO$_2$RR** and **TS-HER** lie at a lower energy than **TS$_{5a\text{-}5b}$**, the tautomerization of species **5b** into **5a** represents the rate-determining step of the whole process within that second regime. Consequently, **5b** is expected to behave as the resting state of the RhCp*@UiO-67 catalyst that accumulates once the concentration of $[Ru(bpy)_3]^+$ is not high enough to permit the direct formation of **5a** from **4a**. Remarkably, the barrier to reach **TS$_{5a\text{-}5b}$** from **5b** (26.0 kcal mol^{-1}) is significantly higher than those for the hydride transfer to both CO_2 and $HTEOA^+$ (15.6 and 14.6 kcal mol^{-1}, respectively). This is consistent with the presence of two regions in the experimental kinetic evolution of formate and H_2 products (Figure 1b), whereby changing slopes (going from steeper to flatter) reflects the change of pathway.[26] Thus, in agreement with the experimental observations, our DFT calculations indicate that these two regions correspond to conditions of high and low concentration of the photosensitizer, respectively.

3. Role of PW_{12} in boosting the photoreduction of CO_2 and H^+ catalyzed by (PW_{12},RhCp*)@UiO-67.

DFT calculations. Previous DFT calculations on the (PW_{12},RhCp*)@UiO-67 system showed that the LUMO of the POM is lower in energy than that of **1**.[26] This suggests the POMs immobilized in the material are more prone to accept electrons than the Rh catalyst itself. Indeed, our DFT calculations indicate that the **PW_{12}→PW_{12}(1e)** reduction by $[Ru(bpy)_3]^+$ is more exergonic but also slightly faster than that of **1→2** (ΔG = -23.2 vs -16.0 kcal mol^{-1} and $\Delta G^‡$ = 5.0 vs 5.7 kcal mol^{-1}, respectively). Besides, **PW_{12}(1e)** is found to be oxidizing enough to spontaneously accept a second electron from $[Ru(bpy)_3]^+$ (ΔG = -8.2 kcal mol^{-1}), forming **PW_{12}(2e)** through a higher but still accessible free-energy barrier of 10.4 kcal mol^{-1}. According to this, the second reduction of the POM might take place after the reduction of **1** into **3**, which proceeds through faster SET steps with free-energy barriers <10 kcal mol^{-1} (see Scheme S2 and Table S2).

Figure 5 summarizes the key steps that take place in the POM-containing system. Interestingly, the **PW_{12}(2e)** anion immobilized near the Rh-catalyst in the pores of (PW_{12},RhCp*)@UiO-67 is capable of reducing **4a** into **5a** through a SET that is exergonic by 5.0 kcal mol^{-1} and gives and **PW_{12}(1e)**. This process (left, green arrows) takes place through a lower free-energy barrier than the proton-hydride tautomerization (left, red arrows) to give **4b**. Importantly, this indicates that, akin to $[Ru(bpy)_3]^+$, **PW_{12}(2e)** can also assist the formation of **5a** while bypassing that of the highly stable intermediate **5b**, allowing **5a** to proceed through the hydride transfer step to yield the products (Figures 4 and 5, right). Note that although reduced POMs are susceptible to associate protons in organic solvents to stabilize the excess of negative charge,[7] the basicity of nitrogen centers of TEOA is stronger than that of oxygen atoms of the POM, which prevents the protonation of the reduced POMs in the MOF. As a matter of fact, the protonation of

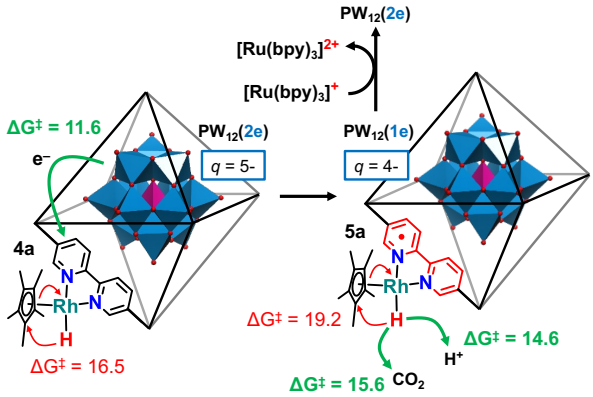

Figure 5. Schematic representation of the key steps involved in the photocatalytic reduction of CO_2 and H^+ by the POM-containing (PW_{12},RhCp*)@UiO-67 catalyst. Gibbs free-energy barriers are given in kcal mol^{-1}.

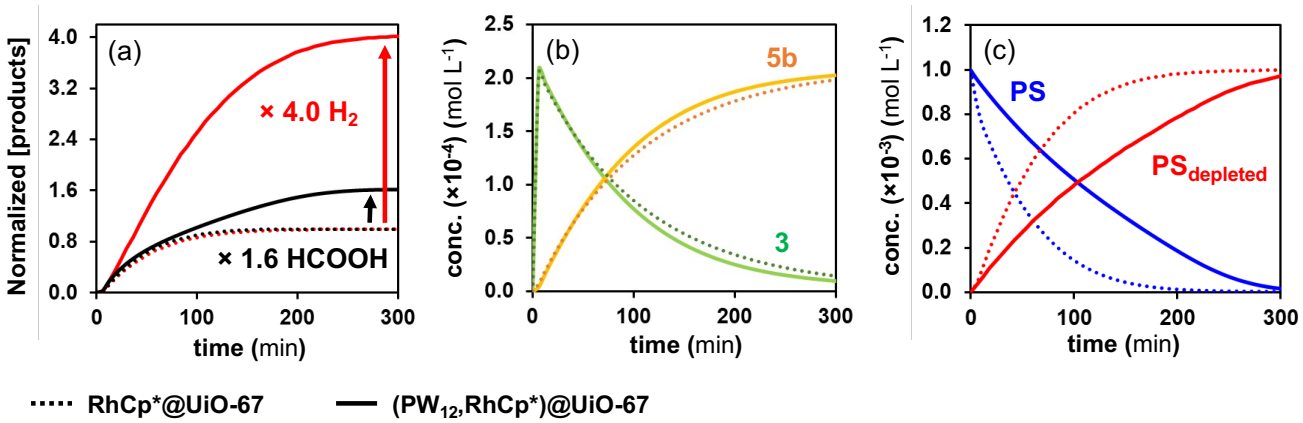

Figure 6. Evolution of the concentrations of (a) HCOOH (black lines) and H_2 (red lines) products, (b) major forms of the catalyst (see Figure S5 for other, low-concentration species), and (c) active and depleted forms of the photosensitizer (PS), along reaction time for the POM-free and the POM-containing systems (dotted and solid lines, respectively). The concentrations of the products were normalized over the maximum production attained by the POM-free system, and that of HCOOH is expressed as the sum of [$HCOO^-$···TEOA], [HCOOH···TEOA] and free [HCOOH] in solution.

PW_{12}(2e) by $HTEOA^+$ is endergonic by 10.4 kcal mol^{-1}. It is also worth mentioning that **PW_{12}(1e)** is not reducing enough to promote the reduction of the catalyst and as such, its reoxidation to **PW_{12}** is not expected to occur during the reaction.

Overall, the above results raise two possible hypotheses to explain the enhancement in the CO_2RR and HER catalytic activity observed for the POM-containing system.

On the one hand, the ability of the POM to act as an electron relay may limit the formation of the resting state **5b** via boosting the direct reduction of **4a** into **5a** when compared to the POM-free-system, in which the rate of this process depends on the encounter probability between $[Ru(bpy)_3]^+$ and the intermediate **4a**. Therefore, the direct reduction of **4a** into **5a**, which allows forming the products through lower energy barriers (Figure 5, vide supra), is more efficient in (**PW_{12}**,RhCp*)@UiO-67 than in the POM-free system since **PW_{12}(2e)** anions are immobilized in close contact with the catalyst.

On the other hand, the decomposition of $[Ru(bpy)_3]^{2+}$ and its reduced form triggered by light is a known process, which has been proposed to involve the population of metal-centered excited states that prompt the loss of bpy ligands.[34,48-50] We recall to the fact that the light-driven formation of formate and H_2 by (**PW_{12}**,RhCp*)@UiO-67 is limited by the decomposition of the photosensitizer,[26] a phenomenon that had been observed before in other systems.[43,45,69-71] Thus, it is also reasonable to propose that the **PW_{12}(1e)** species, which is regenerated over the cycles via a SET from **PW_{12}(2e)** to the catalyst, could act as an additional quencher of $[Ru(bpy)_3]^+$, regenerating $[Ru(bpy)_3]^{2+}$ and preventing in turn, its unproductive decomposition to a higher extent than in the POM-free material. Notably, this hypothesis is consistent with the higher selectivity towards H_2 observed with the POM-containing system. As every molecule of photosensitizer would be able to undergo a greater number of [photoexcitation - reductive quenching - reoxidation] cycles before decomposing, this might lead to a higher concentration of $HTEOA^+$ in solution (see Figure S1), thus favoring the HER over the CO_2RR.

Microkinetic modelling. To evaluate the validity of these hypotheses, we next developed microkinetic models using the rate constants obtained from the DFT-derived free-energy barriers and the reported experimental initial concentrations for our system.[26] The rate constants for processes involving photons, including the photogeneration of $[Ru(bpy)_3]^+$ and the photoinduced decomposition of both $[Ru(bpy)_3]^{2+}$ and $[Ru(bpy)_3]^+$, were empirically fitted to reproduce the experimental behavior of the POM-free system (see SI for details). The same rate constants were then applied in the microkinetic model for the POM-containing catalyst, allowing comparison between both systems. As shown in Figure 6a, the resulting models can nicely reproduce the experimental increase of activity upon incorporating **PW_{12}** in the RhCp*@UiO-67 material, as well as its stronger impact on the HER pathway than on the CO_2RR one. The predicted 1.6- and 4-fold increase of the HCOOH and H_2 yields after 300 min is in nearly quantitative agreement with the experimental values of ca. 2 and 2.5, respectively.[26] Note that the product selectivity is very sensitive to the difference in free-energy between **TS-CO_2RR** and **TS-HER** (see Figure 4). This was estimated as 1 kcal mol^{-1}, which falls well within limits of computational uncertainty. Thus, the overestimation of the H_2:HCOOH ratio lies within the expected margin of error of our calculations. Even so, the overall 2.8-fold increase of activity in terms of products formation predicted by our models is rather aligned with the experimental factor of 2.3, further validating the ability of the models to predict the enhancement in photocatalytic activity granted by the POMs. Remarkably, disabling the electron transfer from **PW_{12}(2e)** to **4a** in the microkinetic model results in product yields comparable to those obtained with POM-free catalyst (Figure S4), indicating that this step is indeed crucial for the POM to improve the performance of the catalyst. Also of note, disabling the electron transfer from $[Ru(bpy)_3]^+$ to **4a** in the POM-free system results in almost no activity at all, as only the red line pathway in Figure 4 is allowed, whereas it only causes a slight decrease of the activity in the POM-containing system (Figure S4). This indicates that in the POM-containing catalyst, both pathways in which the reduced POM and the reduced PS promote the reduction of **4a** into **5a** are operative.

Microkinetic modelling allows not only studying the rate of products formation, but also tracking the concentration of every single species involved in the reaction mechanism over time. A deeper analysis of the time evolution of reaction intermediates revealed that the presence of the POM does not significantly alter the rate at which the resting state accumulates (Figure 6b). However, it is found to have a much stronger impact on the decay of the $[Ru(bpy)_3]^{2+}$ concentration over time (Figure 6c). The POM-containing system

displays a significantly slower conversion of the active photosensitizer (labeled as PS) into its depleted form(s) ($PS_{depleted}$), the latter no longer participating in the reaction.[26] Therefore, we may conclude that the encapsulated POMs play the key role of limiting the degradation of the $[Ru(bpy)_3]^{2+}$ photosensitizer. In conclusion, the various beneficial impacts of the POM may be thus envisioned as follows:

- The POMs act as electron reservoirs by accepting and storing electrons from the reduced photosensitizer, favoring the regeneration of $[Ru(bpy)_3]^{2+}$ over the non-productive decomposition of $[Ru(bpy)_3]^{+}$, which prevails in the absence of POMs due to a lower concentration of electron acceptors (see Figure 6c).
- The above allows the concentration of $[Ru(bpy)_3]^{2+}$ and its reduced partner to be high enough to proceed through the fast reaction pathway (solid lines in Figure 5) for a longer time, resulting in an increase of the products yield.
- Finally, the reduced POMs (**PW_{12}(2e)**) release electrons to the catalysts at the required stage of the catalytic cycle, giving back the oxidized POMs (**PW_{12}(1e)**) that can keep on accepting electrons from $[Ru(bpy)_3]^{+}$. Along this line, it has to be pointed out that, increasing the catalytic activity is mechanistically linked to a decrease of the selectivity towards HCOOH, as the concentration of $HTEOA^{+}$, which is the proton source, increases with the number of catalytic cycles in which $[Ru(bpy)_3]^{2+}$ can participate before decomposing.

To validate our conclusions, we finally reproduced the photocatalytic CO_2-reduction experiments reported in ref. 26 (Figure 1b) using RhCp*@UiO-67 and (**PW_{12}**,RhCp*)@UiO-67 as catalysts ($\lambda \geq$ 415 nm, in 5:1 (v/v) CH_3CN:TEOA solutions containing $[Ru(bpy)_3]^{2+}$ as PS, see Experimental Section) and compared the evolution of the experimental UV-Vis spectra of the reaction mixture over time for the POM-containing and the POM-free catalysts. In striking agreement with our findings, Figure 7 shows a slower decay of the spectral features of $[Ru(bpy)_3]^{2+}$ (maximum absorbance at 455 nm) in the presence of (**PW_{12}**,RhCp*)@UiO-67, compared to those collected with the POM-free system (see Figure S6 for a comparison of the time-evolution of the UV-Vis spectra). This further confirms that POM guests enhance the activity of the material by limiting the degradation of the PS.

4. Impact of the nature of the POM guest: Structure-activity relationships.

Prompted by the ability of our kinetic models to predict variations of both catalytic activity and product selectivity upon the presence of POM in the material, we next conducted a systematic exploration whereby a series of various POMs is evaluated aiming to set structure-activity relationships for CO_2RR and HER performances. Aside from **PW_{12}**, the series of POMs include an array of Keggin-type anions: $[SiW_{12}O_{40}]^{4-}$, **SiW_{12}**; $[AlW_{12}O_{40}]^{5-}$, **AlW_{12}**; $[H_2W_{12}O_{40}]^{6}$, **H_2W_{12}**; the $[H_2PTi_2W_{10}O_{40}]^{5-}$, **$H_2PTi_2W_{10}$**; $[PMo_{12}O_{40}]^{3-}$, **PMo_{12}**; $[SiMo_{12}O_{40}]^{4-}$, **$SiMo_{12}$** and $[PV_2Mo_{10}O_{40}]^{5-}$, **PV_2Mo_{10}**; the Lindqvist-type $[W_6O_{19}]^{2-}$, **W_6**; and the decatungstate $[W_{10}O_{32}]^{4-}$, **W_{10}** anion.

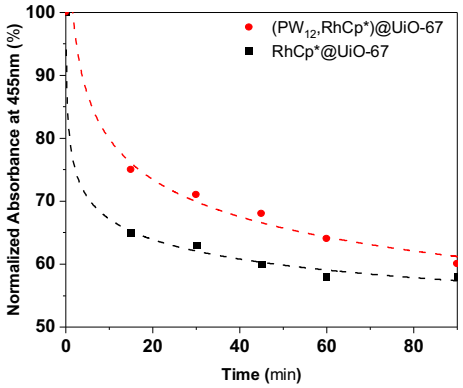

Figure 7. Experimental decrease of the absorbance at 455 nm over time of the reaction mixture (5:1 (v/v) CH_3CN:TEOA containing 0.5 mM of $Ru(bpy)_3Cl_2$) during photocatalytic experiments using (**PW_{12}**,RhCp*)@UiO-67 (red line) and RhCp*@UiO-67 (black line) catalysts.

As discussed in the previous section, a crucial condition for boosting the catalytic activity of a (POM,cat)@MOF system is that the encapsulated POMs must be capable of both accepting an electron from the reduced PS and transferring it to the catalyst (species **4a**) in an exergonic fashion or with an affordable free-energy cost. Table S5 compiles the ΔG values for both SET processes calculated for all the selected POMs and considering multiple redox states. All tested polyoxomolybdates are not suitable for acting as electron relay as their reduced form may not reduce the catalyst, in line with their low-energy laying d-band.[7] Among the rest of POMs, we found that and identified 7 redox pairs (including 1 and 2 electron-reduced forms) that do fulfill the aforementioned condition: **SiW_{12}(0/1e)**, **W_{10}(0/1e)**, **PW_{12}(1/2e)**, **AlW_{12}(0/1e)**, **SiW_{12}(1/2e)**, **$H_2PTi_2W_{10}$(0/1e)** and **W_6(0/1e)**. Further studies were thus conducted with these POMs only. Specifically, we determined the free-energy barriers for the SET steps (Table S5), which allowed us to predict the catalytic behavior of the related (POM,cat)@MOF materials using our microkinetic models. For comparison, we also included here the **H_2W_{12}(0/1e)** pair, which performance might be limited by the cost of **H_2W_{12}** reduction by $[Ru(bpy)_3]^{+}$ (ΔG_{SET} = +7.9 kcal mol^{-1}) and **PW_{12}(0/1e)**, which activity is hampered by **PW_{12}(1e)** not being able to spontaneously reduce the catalyst (ΔG_{SET} = +10.0 kcal mol^{-1}). In all cases, the loading of POM inside the material was assumed to be the same as in (**PW_{12}**,RhCp*)@UiO-67.[26]

Figure 8 plots the predicted catalytic activities of the (POM,RhCp*)@UiO-67 systems expressed as the total product yields after 300 min and normalized by that of the POM-free RhCp*@UiO-67, against the reduction potential of the POM (see Table S6 for values). Interestingly, the distribution of catalytic activities does not follow a linear relationship with the reduction potential of the POM, but rather describes a volcano-type dependence. The highest impact on the catalytic activity (almost 3 times that of the POM-free system) was found for POMs with a moderate reduction potential (ranging from ca. -0.6 to -0.8 V vs NHE). By far, the highest activities are predicted for the (**W_{10}**,RhCp*)@UiO-67 and our experimentally-tested (**PW_{12}**,RhCp*)@UiO-67 system which shows a high selectivity for H_2 (see Figure S8). The other POMs with either higher or lower potentials within a range of ca. 200 mV (i.e. **W_6**, **AlW_{12}**, and **SiW_{12}**) can still provide a higher catalytic activity than that of the POM-free system, although a less pronounced enhancement is predicted (by a factor of ~1.3-1.9; see

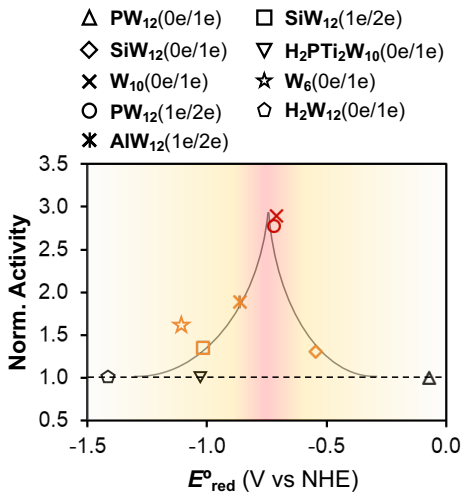

Figure 8. Volcano-plot of the catalytic activity of (**POM**,RhCp*)@UiO-67 catalysts normalized by that of the RhCp*@UiO-67 system vs the redox potential of the encapsulated POM. Gray lines are depicted to guide the eye.

Figure 8). This further evidences that enhancing the catalytic activity of (**POM**,cat)@MOF catalysts requires the POM to have a balanced ability to accept electrons from the reduced PS with that of transferring them to the catalyst. Indeed, as shown in Figure S9, the highest activity is reported for POMs that simultaneously minimize the free-energy barriers for both SET steps, whereas POMs with too high and too low redox potentials cannot be efficiently reduced by the PS or their reduced partner is not reducing enough for activating the catalyst. Nevertheless, some of the POMs with moderate impact of the overall catalytic activity, such as **W$_6$** or **AlW$_{12}$**, could give access to a formate production comparable to that of (**PW$_{12}$**,RhCp*)@UiO-67, in conjunction with a lower amount of H_2 (see Figure S8), hence providing improved selectivity towards CO_2RR compared to (**PW$_{12}$**,RhCp*)@UiO-67.

Importantly, the structure-activity relationships described in Figure 8 can be used as a generic approach to evaluate a whole variety of redox-active guests inside porous catalytic hosts and edit general rules for targeting guests with beneficial impact on the activity of the whole photocatalytic system. In general, the reduction potentials of the PS and the catalyst determine the top and bottom limits of the region where the redox potential of the guest should lie in order to boost the catalytic activity. Bearing this in mind, the theoretical, optimal activity is reached when the redox potential of the guest is halfway between those of the catalyst and the PS. Nevertheless, the location of this optimum is expected to slightly vary depending on the reorganization energies involved in the SET steps (PS to guest and guest to catalyst), which influences the relative rate of both processes. Overall, the herein reported trends might serve as a guideline to rationally develop the next generations of host-guest and, more generally, of multi-component catalytic systems with tailored activity and selectivity under photocatalytic conditions.

CONCLUSIONS

The beneficial role of immobilizing polyoxometalates near catalytic sites for boosting their photocatalytic activity is elucidated by a comprehensive approach combining DFT calculations and microkinetic modelling techniques, supplemented by photophysical and spectroscopic experimental measurements. We selected here the recent experimentally-tested (**PW$_{12}$**,RhCp*)@UiO-67 catalytic material, known to outperform its POM (**PW$_{12}$**)-free analogue in the visible-light driven reduction of CO_2 and H^+ to HCOOH and H_2, respectively, in the presence of $[Ru(bpy)_3]^{2+}$ as an external photosensitizer and TEOA as a sacrificial donor.[26] Our mechanistic investigations first show that the **PW$_{12}$** POM inside this MOF acts as an efficient electron reservoir, accepting electrons from the photo-reduced PS, $[Ru(bpy)_3]^{+}$, and transferring them to the Rh catalyst in the MOF to generate its active form. Secondly, the comparison of the POM-free and POM-containing catalysts by means of microkinetic models correctly predicts the experimental trends in term of boosting yields and observed selectivities, while revealing that storing electrons in the POMs benefits the overall catalytic activity by favoring the regeneration of the oxidized PS, $[Ru(bpy)_3]^{2+}$, over its unproductive degradation, the latter being a usual limitation of the activity of the system. This boosts the overall activity by allowing the PS to participate in a greater number of catalytic cycles before it decomposes. Finally, the reduced POMs are reoxidized by transferring electrons to the catalytic sites. Indeed, experiments confirmed a slower degradation of the PS in the presence of **PW$_{12}$** in the material. Still, as the activity increases, so does the selectivity towards H_2, since a higher concentration of protons is generated through the reductive quenching of the photoexcited photosensitizer by TEOA.

Finally, we have further undertaken a systematic investigation of the potential impact of a series of POMs with different compositions on the overall catalytic activity of analogue (**POM**,cat)@MOF systems. A volcano plot that correlates the photocatalytic activity of the (POM,cat) pair with the reduction potential of the POM is identified. Besides predicting POMs with potential ability to tune the activity and selectivity of the catalyst for CO_2RR and HER, this analysis reveals that a sweet spot is reached when a balance between the ability of the POM to be reduced by the PS and the ability of its reduced form to transfer an electron to the catalyst is attained.

Overall, we provide for the first time a complete picture of the processes governing the photocatalytic activity of a (**POM**,cat)@MOF material, which allowed rationalizing the boost in its CO_2RR and HER performances observed upon encapsulating POMs inside the pores of the RhCp*@UiO-67 catalyst. Most importantly, we established structure-activity relationships that are POM-chemistry independent; i.e. activity vs redox potential of the guest. We expect these results to pave the way for the rational design of novel, porous heterogeneous catalysts and assembled multi-component photocatalytic platforms with enhanced activity and tailored selectivity, inspiring the scientific community in photocatalysis towards the use not only of POMs, but also of other types of redox-active mediators.

METHODS

Computational Details. DFT calculations were carried out at the ωB97X-D level[72] using the Gaussian16 (rev C01) quantum chemistry package.[73] Such level of theory has proved good agreement with experimental data concerning reaction mechanisms, including both kinetic and thermodynamic features.[74-76] Also, the energies obtained with this functional for steps involving variations of overall charge and multiplicity do not differ significantly from those obtained with other GGA and meta-GGA functionals (see Table S8). The LANL2DZ basis set and associated pseudopotentials[77] were used to describe Rh, Ru, W, Mo, V, and Ti centers. These were supplemented by a Frenking's f-type polarization functions.[78] The remaining atoms were treated with the all-electron 6-31G(d,p) basis set.[79-81] Increasing the dimension of the basis set up to triple-ζ quality does

not significantly alter the results (Figure S11). Solvent effects of acetonitrile were included in geometry optimizations and energy calculations by means of the IEF-PCM implicit solvent model,[82] as implemented in Gaussian16. Calculations on the RhCp*@UiO-67 system were carried out with models consisting in a RhCp*-containing linker, where terminal carboxylate groups were saturated with hydrogen atoms (see Figure S12). Geometry optimizations were full and without any symmetry restriction. The nature of all the stationary points on the potential energy surface was confirmed by frequency calculations. A data set collection of the optimized structures for the most representative species is available in the ioChem-BD repository[83] and can be accessed via doi.org/10.19061/iochem-bd-6-128. Unless otherwise noted, Rh complexes were modeled in their lowest M_S value, according to previous computational studies on homogeneous RhCp* derivatives.[29] Further details of their electronic structure can be found in Figures S13 and S14. The standard-state correction of +1.89 kcal mol^{-1} was applied to the free energy of all the species. This accounts for the free-energy variation in going from the reference state of an ideal gas at 1 atm used by Gaussian to the standard state of 1 mol L^{-1} in solution at 298.15 K. ωB97X-D-derived redox potentials in acetonitrile were corrected by applying a rigid shift obtained from comparison with experimental values (see SI for details). Microkinetic analyses were performed using the Acuchem software[84] for solving the differential rate equations. Rate constants for elementary steps were obtained from the calculated standard state free-energy barriers and using the Eyring's equation, while initial concentrations were set to reproduce the experimental conditions.[26] Free-energy barriers for SET processes were estimated by means of the Marcus theory of the electron transfer,[85,86] as adapted by Vaissier et al.[87] Further details about the microkinetic models and the application of the Marcus theory are provided in the SI.

Transient absorption spectroscopy. Nanosecond transient absorption measurements were performed on a home-built setup, which has been described previously.[88] Briefly, a Nd:YAG pumped optical parametric oscillator (OPO) laser is used for sample excitation at 460 nm with an energy of ~ 2 mJ/pulse with a repetition rate of 10Hz. After excitation, the sample is probed by a white light continuum laser (LEUKOS) in a repetition rate of 20 Hz. The probe beam is split into two arms, one for probing sample and the other for reference in order to compensate for energy fluctuations. The probing arm is coupled, after passing the sample, into a round to linear optical fiber bundle, before being analyzed by a spectrograph SPEX 270M (Jobin-Yvon). Detection of the dispersed white light is performed by an intensified CCD (ICCD) detector PIMAX 4 (Princeton Instrument). Transient absorption spectra were calculated using the following formula:

$$\Delta OD = \log_{10}\left(\frac{S_{ref}^{on}}{S_{ref}^{off}} \times \frac{S_{prob}^{off}}{S_{prob}^{on}}\right)$$

where S_{ref}^{on} and S_{ref}^{off} are reference spectra when pump laser is on and off respectively, S_{prob}^{on} and S_{prob}^{off} are probe spectra when pump laser is on and off, respectively.

Photo-irradiation experiments. Photo-irradiation experiments were performed in a 1 cm optical path quartz cuvette in Ar-saturated solutions. Analytik Jena Specord spectrometer was used to probe the sample. The sample was irradiated with a 456 nm LED light source with ~ 60 mW/cm^2 output (Kessil PR160L).

General photochemical procedure. RhCp*@UiO-67 and (**PW_{12}**,RhCp*)@UiO-67 were prepared and characterized as described in ref. 26. A 5:1 CH_3CN/TEOA mixture was used as a solvent (CH_3CN and TEOA purchased from Sigma-Aldrich and used without further purification). The photosensitizer utilized was a 0.5 mM solution of $Ru(bpy)_3Cl_2$ (purchased from Sigma-Aldrich used without further purification). 1.4 mg of (**PW_{12}**,RhCp*)@UiO-67 and 0.9 mg of RhCp*@UiO-67, which corresponds to 0.17 μmol of RhCp* catalyst, were used for the photocatalytic studies. Samples were saturated with CO_2 via directly bubbling CO_2 through the solution mixture for 20 min. During irradiation, the samples were vigorously stirred and 100μL of solution were taken at different time. The reaction mixture was diluted 10 time and centrifuged before recording UV-Vis spectra. Photochemical reactions were performed using a 280 W, high pressure Xe arc lamp (Newport Instruments). The beam was passed through a water infrared filter, a collimating lens, and a filter holder equipped with a 415 nm band-pass filter (Asahi Spectra). Samples were prepared in a 1 cm path length quartz sealed cuvette (Hellma) which was placed in a temperature-controlled cuvette holder (Quantum Northwest) maintained at 20 °C with a circulated water bath. UV–vis spectra were recorded on a PerkinElmer Lambda 750 UV/vis/NIR spectrometer.

AUTHOR INFORMATION

Corresponding Author

* E-mail: caroline.mellot-draznieks@college-de-france.fr, a.sole-daura@uva.nl

Present Addresses

† Van't Hoff Institute for Molecular Sciences, University of Amsterdam, 1098 XH Amsterdam, The Netherlands.

Author Contributions

The manuscript was written through contributions of all authors. All authors have given approval to the final version of the manuscript.

Funding Sources

This work was supported by CNRS and UVSQ. The calculations have been performed using the HPC national resources from GENCI (CINES/TGCC/) through 2021 Grant A0090907343.

ABBREVIATIONS

DFT, density functional theory; POM, polyoxometalate; MOF, metal-organic framework; TM, transition metal; CO_2RR, carbon dioxide reduction reaction; HER, hydrogen evolution reaction; TEOA, triethanolamine; PS, photosensitizer; NHE, normal hydrogen electrode; SET, single electron transfer; MLCT, metal-to-ligand charge transfer; UV-Vis, ultraviolet-visible; LED, light-emitting diode; TAS, transient absorption spectroscopy.

ASSOCIATED CONTENT

Supporting Information. Differential UV-vis spectra, energetics for the initial reduction steps, additional TAS experiments, details about the microkinetic models, compilation of energetic parameters for other POMs, results from microkinetic analyses with other (POM,cat)@MOF systems, details about the application of the Marcus theory of the electron transfer (PDF). This material is available free of charge via the Internet at http://pubs.acs.org.

REFERENCES

(1) Aresta, M. Carbon Dioxide as Chemical Feedstock; WILEY-VCH Verlag GmbH & Co. KGaA, Weinheim, 2010.

(2) Otto, A.; Grube, T.; Schiebahn, S.; Stolten, D. Closing the loop: captured CO_2 as a feedstock in the chemical industry. *Energy Environ. Sci.* **2015**, *8*, 3283-3297

(3) Li, K.; An, X.; Park, K. H.; Khraisheh, M.; Tang, J. A critical review of CO_2 photoconversion: Catalysts and reactors. *Catal. Today* **2014**, *224*, 3–12.

(4) Hao, Y.; Steinfeld, A. Fuels from water, CO_2 and solar energy. *Sci. Bull.* **2017**, *62*, 1099–1101.

(5) Pope, T. Heteropoly and Isopoly Oxometalates, Springer, New York, 1983.

(6) Long, D. L.; Tsunashima, R.; Cronin, L. Polyoxometalates: building blocks for functional nanoscale systems. *Angew. Chem. Int. Ed.* **2010**, 49, 1736–1758.

(7) López, X.; Carbó, J. J.; Bo, C.; Poblet, J. M. Structure, properties and reactivity of polyoxometalates: a theoretical perspective. *Chem. Soc. Rev.* **2012**, *41*, 7537-7571.

(8) Pope, M. T.; Müller, A. Polyoxometalate chemistry: an old field with new dimensions in several disciplines. *Angew. Chem., Int. Ed. Engl.* **1991**, *30*, 34–38.

(9) Kawasaki, N.; Wang, H.; Nakanishi, R.; Hamanaka, S.; Kitaura, R.; Shinohara, H.; Yokoyama, T.; Yoshikawa, H.; Awaga, K. Nanohybridization of polyoxometalate clusters and single-wall carbon nanotubes: applications in molecular cluster batteries. *Angew. Chem., Int. Ed.* **2011**, *123*, 3533–3536.

(10) Chen, J.-J.; Symes, M. D.; Cronin, L. Highly reduced and protonated aqueous solutions of $[P_2W_{18}O_{62}]^{6-}$ for on-demand hydrogen generation and energy storage. *Nat. Chem.* **2018**, *10*, 1042–1047.

(11) Streb, C.; Kastner, K.; Tucher, J. Polyoxometalates in photocatalysis. *Phys. Sci. Rev.* **2019**; 20170177.

(12) Ettedgui, J.; Diskin-Posner, Y.; Weiner, L.; Neumann, R. Photoreduction of Carbon Dioxide to Carbon Monoxide with Hydrogen Catalyzed by a Rhenium(I) Phenanthroline–Polyoxometalate Hybrid Complex. *J. Am. Chem. Soc.* **2011**, *133*, 188–190.

(13) Ci, C.; Carbó, J. J.; Neumann, R.; de Graaf, C.; Poblet, J. M. Photoreduction Mechanism of CO_2 to CO Catalyzed by a Rhenium(I)–Polyoxometalate Hybrid Compound. *ACS Catal.* **2016**, *6*, 6422–6428.

(14) Yu, H.; Haviv, E.; Neumann, R. Visible-Light Photochemical Reduction of CO_2 to CO Coupled to Hydrocarbon Dehydrogenation. *Angew. Chem. Int. Ed.* **2020**, *132*, 6278-6282.

(15) Wang, F.; Neumann, R.; de Graaf, C.; Poblet, J. M. Photoreduction Mechanism of CO_2 to CO Catalyzed by a Three-Component Hybrid Construct with a Bimetallic Rhenium Catalyst. *ACS Catal.* **2021**, *11*, 1495–1504.

(16) Liu, S.-M.; Zhang, Z.; Li, X.; Jia, H.; Ren, M.; Liu, S. Ti-Substituted Keggin-Type Polyoxotungstate as Proton and Electron Reservoir Encaged into Metal–Organic Framework for Carbon Dioxide Photoreduction. *Adv. Mater. Interfaces* **2018**, 1801062.

(17) Gu, J.; Chen, W.; Shan, G.-G.; Li, G.; Sun, C.; Wang, X.-L.; Su, Z. The roles of polyoxometalates in photocatalytic reduction of carbon dioxide. *Mater. Today Energy* **2021**, *21*, 100760.

(18) Sun, M.-L.; Wang, Y.-R.; He, W.-W.; Zhong, R.-L.; Liu, Q.-Z.; Xu, S.; Xu, J.-M.; Han, X.-L.; Ge, X.; Li, S.-L.; Lan, Y.-Q.; Al-Enizi, A. M.; Nafady, A.; Ma, S. Efficient Electron Transfer from Electron-Sponge Polyoxometalate to Single-Metal Site Metal–Organic Frameworks for Highly Selective Electroreduction of Carbon Dioxide. *Small* **2021**, 2100762.

(19) Lang, Z.; Miao, J.; Lan, Y.; Cheng, J.; Xu, X.; Cheng, C. Polyoxometalates as electron and proton reservoir assist electrochemical CO_2 reduction. *APL Mater.* **2020**, *8*, 120702.

(20) Guo, W.; Lv, H.; Chen, Z.; Sullivan, K. P.; Lauinger, S. M.; Chi, Y.; Sumliner, J. M.; Liana, T.; Hill, C. L. Self-assembly of polyoxometalates, Pt nanoparticles and metal–organic frameworks into a hybrid material for synergistic hydrogen evolution. *J. Mater. Chem. A* **2016**, *4*, 5952-5957.

(21) Tian, P.; He, X.; Li, W.; Zhao, L.; Fang, W.; Chen, H.; Zhang, F.; Zhang, W.; Wang, W. Zr-MOFs based on Keggin-type polyoxometalates for photocatalytic hydrogen production. *J. Mat. Sci.* **2018**, *53*, 12016–12029.

(22) Liu, R.; Zhang, G.; Cao, H.; Zhang, S.; Xie, Y.; Haider, A.; Kortz, U.; Chen, B.; Dalal, N. S.; Zhao, Y.; Zhi, L.; Wu, C.-X.; Yan, L.-K.; Su, Z.; Keita, B. Enhanced proton and electron reservoir abilities of polyoxometalate grafted on graphene for high-performance hydrogen evolution. *Energy Environ. Sci.* **2016**, *9*, 1012-1023.

(23) Liu, Y.; Tang, C.; Cheng, M.; Chen, M.; Chen, S.; Lei, L.; Chen, Y.; Yi, H.; Fu, Y.; Li, L. Polyoxometalate@Metal-Organic Framework Composites as Effective Photocatalysts. *ACS Catal.* **2021**, *11*, 13374–13396.

(24) Mialane, P.; Mellot-Draznieks, C.; Gairola, P.; Duguet, M.; Benseghir, Y.; Oms O.; Dolbecq, A. Heterogenisation of polyoxometalates and other metal-based complexes in metal–organic frameworks: from synthesis to characterisation and applications in catalysis. *Chem. Soc. Rev.* **2021**, *50*, 6152-6220.

(25) Samaniyan, M.; Mirzaei, M.; Khajavian, R.; Eshtiagh-Hosseini, H.; Streb, C. Heterogeneous Catalysis by Polyoxometalates in Metal-Organic Frameworks. *ACS Catal.* **2019**, *9*, 10174–10191.

(26) Benseghir, Y.; Lemarchand, A.; Duguet, M.; Mialane, P.; Gomez-Mingot, M.; Roch-Marchal, C.; Pino, T.; Ha-Thi, M.-H.; Haouas, M.; Fontecave, M.; Dolbecq, A.; Sassoye, C.; Mellot-Draznieks, C. Co-immobilization of a Rh Catalyst and a Keggin Polyoxometalate in the UiO-67 Zr-Based Metal–Organic Framework: In Depth Structural Characterization and Photocatalytic Properties for CO_2 Reduction. *J. Am. Chem. Soc.* **2020**, *142*, 9428–9438.

(27) Caix, C.; Chardon-Noblat, S.; Deronzier, A. Electrocatalytic reduction of CO_2 into formate with $[(\eta^5\text{-}Me_5C_5)M(L)Cl]^+$ complexes (L = 2,2′-bipyridine ligands; M = Rh(III) and Ir(III)). *J. Electroanal. Chem.* **1997**, *434*, 163-170.

(28) Chambers, M. B.; Wang, X.; Elgrishi, N.; Hendon, C. H.; Walsh, A.; Bonnefoy, J.; Canivet, J.; Quadrelli, E. A.; Farrusseng, D.; Mellot-Draznieks, C.; Fontecave, M. Photocatalytic Carbon Dioxide Reduction with Rhodium-based Catalysts in Solution and Heterogenized within Metal–Organic Frameworks. *ChemSusChem* **2015**, *8*, 603–608.

(29) Todorova, T. K.; Huan, T. N.; Wang, X.; Agarwala, H.; Fontecave, M. Controlling Hydrogen Evolution during Photoreduction of CO_2 to Formic Acid Using $[Rh(R\text{-}bpy)(Cp^*)Cl]^+$ Catalysts: A Structure-Activity Study. *Inorg. Chem.* **2019**, *58*, 6893–6903.

(30) Wang, X.; Wisser, F. M.; Canivet, J.; Fontecave, M.; Mellot-Draznieks, C. Immobilization of a Full Photosystem in the Large-Pore MIL-101 Metal–Organic Framework for CO_2 Reduction. *ChemSusChem* **2018**, *11*, 3315–3322.

(31) Caix, C.; Chardon-Noblat, S.; Deronzier, A.; Moutet, J.-C.; Tingry, S. (Pentamethylcyclopentadienyl)(polypyridyl) rhodium and iridium complexes as electrocatalysts for the reduction of protons to dihydrogen and the hydrogenation of organics. *J. Organomet. Chem.* **1997**, *540*, 105-111.

(32) Ghosh, D.; Takeda, H.; Fabry, D. C.; Tamaki, Y.; Ishitani, O. Supramolecular Photocatalyst with a Rh(III)-Complex Catalyst Unit for CO_2 Reduction. *ACS Sustain. Chem. Eng.* **2019**, *7*, 2648–2657.

(33) Juris, A.; Balzani, V.; Belser, P.; von Zelewsky, A. Characterization of the Excited State Properties of Some New Photosensitizers of the Ruthenium (Polypyridine) Family. *Helv. Chim. Acta* **1981**, *64*, 2175-2182.

(34) Durham, B.; Caspar, J. V.; Nagle, J. K.; Meyer, T. J. Photochemistry of Tris(2,2′-Bipyridine)Ruthenium(2+) Ion. *J. Am. Chem. Soc.* **1982**, *104*, 4803–4810.

(35) Prier, C. K.; Rankic, D. A.; MacMillan D. W. C. Visible Light Photoredox Catalysis with Transition Metal Complexes: Applications in Organic Synthesis. *Chem. Rev.* **2013**, *113*, 5322–5363.

(36) Redox potentials from ref. (35) and ref. (57) were converted from the SCE to the NHE reference by applying +0.25 V.

(37) Sun, H.; Hoffman, M. Z. Reductive Quenching of the Excited States of Ruthenium(II) Complexes Containing 2,2'-Bipyridine, 2,2'-Bipyrazine, and 2,2'-Bipyrimidine Ligands. *J. Phys. Chem.* **1994**, *98*, 11719-11726.

(38) Goldsmith, J. I.; Hudson, W. R.; Lowry, M. S.; Anderson, T. H.; Bernhard, S. Discovery and High-Throughput Screening of Heteroleptic Iridium Complexes for Photoinduced Hydrogen Production. *J. Am. Chem. Soc.* **2005**, *127*, 7502-7510.

(39) Sun, H.; Hoffman, M. Z. Photo-induced charge separation by ruthenium(ll) photosensitizers. *J. Chem. Sci.* **1993**, *105*, 487–494.

(40) Cline, E. D.; Adamson, S. E.; Bernhard, S. Homogeneous Catalytic System for Photoinduced Hydrogen Production Utilizing Iridium and Rhodium Complexes. *Inorg. Chem.* **2008**, 47, 10378-10388.

(41) Lin, X.; Xie, Z.; Su, B.; Zheng, M.; Dai, W.; Hou, Y.; Ding, Z.; Lin, W.; Fang, Y.; Wang, S. Well-defined Co_9S_8 cages enable the separation of photoexcited charges to promote visible-light CO_2 reduction. *Nanoscale* **2021**, *13*, 18070–18076.

(42) Fujita, E.; Chou, M.; Tanaka, K. Characterization of $Ru(bpy)_2(CO)(COO)$ prepared by CO_2 addition to $Ru(bpy)_2(CO)$ in acetonitrile *Appl. Organometal. Chem.* **2000**, *14*, 844–846.

(43) Gao, C.; Meng, Q.; Zhao, K.; Yin, H.; Wang, D.; Guo, J.; Zhao, S.; Chang, L.; He, M.; Li, Q.; Zhao, H.; Huang, X.; Gao, Y.; Tang, Z. Co_3O_4 Hexagonal Platelets with Controllable Facets Enabling Highly Efficient Visible-Light Photocatalytic Reduction of CO_2. *Adv. Mater.* **2016**, *28*, 6485–6490.

(44) Lehn, J.-M.; Ziessel, R. Photochemical reduction of carbon dioxide to formate catalyzed by 2,2'-bipyridine- or 1,10-phenanthroline-ruthenium(II) complexes. *J. Organomet. Chem.* **1990**, *382*, 157-173.

(45) Lin, X.; Wang, S.; Tu, W.; Wang, H.; Hou, Y.; Dai, W.; Xu, R. Magnetic Hollow Spheres Assembled from Graphene-Encapsulated Nickel Nanoparticles for Efficient Photocatalytic CO_2 Reduction. *ACS Appl. Energy Mater.* **2019**, *2*, 7670–7678.

(46) Mallouk, T. E.; Krueger, J. S.; Mayer, J. E.; Dymond, C. M. G. Reductive quenching of ruthenium polypyridyl sensitizers by cyanometalate complexes. *Inorg. Chem.* **1989**, *28*, 3507–3510.

(47) Rivarola, C. R.; Bertolotti, S. G.; Previtali, C. M. Photoreduction of $Ru(bpy)_3^{+2}$ by Amines in Aqueous Solution. Kinetics Characterization of a Long-Lived Nonemitting Excited State. *Photochem. Photobiol.* **2006**, *82*, 213-218.

(48) Mukuta, T.; Tanaka, S.; Inagaki, A.; Koshihara, S.; Onda, K. Direct Observation of the Triplet Metal-Centered State in $[Ru(bpy)_3]^{2+}$ Using Time-Resolved Infrared Spectroscopy. *ChemistrySelect* **2016**, *1*, 2802–2807.

(49) Soupart, A.; Alary, F.; Heully, J.-L.; Elliott, P. I. P.; Dixon, I. M. Exploration of Uncharted 3PES Territory for $[Ru(bpy)_3]^{2+}$: A New ^{3}MC Minimum Prone to Ligand Loss Photochemistry. *Inorg. Chem.* **2018**, *57*, 3192–3196.

(50) Soupart, A.; Alary, F.; Heully, J.-L.; Elliott, P. I. P. Dixon, I. M. Recent progress in ligand photorelease reaction mechanisms: theoretical insights focusing on Ru(II) ^{3}MC states. *Coord. Chem. Rev.* **2020**, *408*, 213184.

(51) Gueret, R.; Poulard, L.; Oshinowo, M.; Chauvin, J.; Dahmane, M.; Dupeyre, G.; Lainé, P. P.; Fortage, J.; Collomb, M.-N. Challenging the $[Ru(bpy)_3]^{2+}$ Photosensitizer with a Triazatriangulenium Robust Organic Dye for Visible-Light-Driven Hydrogen Production in Water. *ACS Catal.* **2018**, *8*, 3792–3802.

(52) Sampaio, R. N.; Grills, D. C.; Polyansky, D. E.; Szalda, D. J.; Fujita, E. Unexpected Roles of Triethanolamine in the Photochemical Reduction of CO_2 to Formate by Ruthenium Complexes. *J. Am. Chem. Soc.* **2020**, *142*, 2413–2428.

(53) Ghosh, D.; Fabry, D. C.; Saito, D.; Ishitani, O. Photochemical H_2 Evolution Using a Ru–Rh Supramolecular Photocatalyst. *Energy Fuels* **2021**, *35*, 19069–19080.

(54) Cohen, S. G.; Parola, A.; Parsons, G. H. Photoreduction by Amines. *Chem. Rev.* **1973**, *73*, 141–161.

(55) Cohen, S. G.; Baumgarten, R. J. Photoreduction of Benzophenone by Amines. Photochemical Oxidative Deamination. *J. Am. Chem. Soc.* **1965**, *87*, 2996–2997.

(56) Pellegrin, Y.; Odobel, F. Sacrificial Electron Donor Reagents for Solar Fuel Production. *C. R. Chim.* **2017**, *20*, 283–295.

(57) Delaive, P. J.; Foreman, T. K.; Giannotti, C.; Whitten, D. G. Photoinduced electron transfer reactions of transition-metal complexes with amines. Mechanistic studies of alternate pathways to back electron transfer. *J. Am. Chem. Soc.* **1980**, *102*, 5627-5631.

(58) Johnson, B. A.; Bhunia, A.; Fei, H.; Cohen, S. M.; Ott, S. Development of a UiO-Type Thin Film Electrocatalysis Platform with Redox-Active Linkers. J. *Am. Chem. Soc.* **2018**, *140*, 2985–2994.

(59) McCarthy, B. D.; Beiler, A. M.; Johnson, B. A.; Liseev, T.; Castner, A. T.; Ott, S. Analysis of Electrocatalytic Metal-Organic Frameworks. *Coord. Chem. Rev.* **2020**, *406*, 213137.

(60) Mukhopadhyay, S.; Basu, O.; Kar, A.; Das, S. K. Efficient Electrocatalytic Water Oxidation by Fe(salen)–MOF Composite: Effect of Modified Microenvironment. *Inorg. Chem.* **2020**, *59*, 472–483.

(61) Goswami, S.; Ray, D.; Otake, K.; Kung, C.-W.; Garibay, S. J.; Islamoglu, T.; Atilgan, A.; Cui, Y.; Cramer, C. J.; Farha, O. K.; Hupp, J. T. A porous, electrically conductive hexa- zirconium(IV) metal–organic framework. *Chem. Sci.* **2018**, *9*, 4477–4482.

(62) Madsen, M. R.; Rønne, M. H.; Heuschen, M.; Golo, D.; Ahlquist, M. S. G.; Skrydstrup, T.; Pedersen, S. U.; Daasbjerg, K. Promoting Selective Generation of Formic Acid from CO_2 Using $Mn(bpy)(CO)_3Br$ as Electrocatalyst and Triethylamine/Isopropanol as Additives. *J. Am. Chem. Soc.* **2021**, *143*, 20491–20500.

(63) Rønne, M. H.; Cho, D.; Madsen, M. R.; Jakobsen, J. B.; Eom, S.; Escoudé, É.; Hammershøj, H. C. D.; Nielsen, D. U.; Pedersen, S. U.; Baik, M.-H.; Skrydstrup, T.; Daasbjerg, K. Ligand-Controlled Product Selectivity in Electrochemical Carbon Dioxide Reduction Using Manganese Bipyridine Catalysts. *J. Am. Chem. Soc.* **2020**, *142*, 4265–4275.

(64) Margarit, C. G.; Asimow, N. G.; Costentin, C.; Nocera, D. G. Tertiary Amine-Assisted Electroreduction of Carbon Dioxide to Formate Catalyzed by Iron Tetraphenylporphyrin. *ACS Energy Lett.* **2020**, *5*, 72–78.

(65) Quintana, L. M. A.; Johnson, S. I.; Corona, S. L.; Villatoro, W.; Goddard, W. A.; Takase, M. K.; VanderVelde, D. G.; Winkler, J. R.; Gray, H. B.; Blakemore, J. D. Proton–hydride tautomerism in hydrogen evolution catalysis. *Proc. Natl. Acad. Sci. U. S. A.* **2016**, *113*, 6409–6414.

(66) Pitman, C. L.; Finster, O. N. L.; Miller, A. J. M. Cyclopentadiene-mediated hydride transfer from rhodium complexes. *Chem. Commun.* **2016**, *52*, 9105–9108.

(67) Peng, Y.; Ramos-Garcés, M. V.; Lionetti, D.; Blakemore, J. D. Structural and Electrochemical Consequences of [Cp*] Ligand Protonation. *Inorg. Chem.* **2017**, *56*, 10824–10831.

(68) Boyd, E. A.; Lionetti, D.; Henke, W. C.; Day, V. W.; Blakemore, J. D. Preparation, Characterization, and Electrochemical Activation of a Model [Cp*Rh] Hydride. *Inorg. Chem.* **2019**, *58*, 3606–3615.

(69) Wang, S.; Yao, W.; Lin, J.; Ding Z.; Wang, X. Cobalt Imidazolate Metal–Organic Frameworks Photosplit CO_2 under Mild Reaction Conditions. *Angew. Chem., Int. Ed.* **2014**, *53*, 1034–1038.

(70) Niu, P.; Pan, Z.; Wang S.; Wang, X. Tuning Crystallinity and Surface Hydrophobicity of a Cobalt Phosphide Cocatalyst to Boost CO_2 Photoreduction Performance. *ChemSusChem*, **2021**, *14*, 1302–1307.

(71) Boston, D. J.; Xu, C.; Armstrong, D. W.; MacDonnell, F. M. Photochemical reduction of carbon dioxide to methanol and formate in a homogeneous system with pyridinium catalysts. *J. Am. Chem. Soc.* **2013**, *135*, 16252-16255.

(72) Chai, J.-D.; Head-Gordon, M. Long-Range Corrected Hybrid Density Functionals with Damped Atom–Atom Dispersion Corrections. *Phys. Chem. Chem. Phys.* **2008**, *10*, 6615–6620.

(73) Gaussian 16, Revision C.01, Frisch, M. J.; Trucks, G. W.; Schlegel, H. B.; Scuseria, G. E.; Robb, M. A.; Cheeseman, J. R.; Scalmani, G.; Barone, V.; Petersson, G. A.; Nakatsuji, H.; Li, X.; Caricato, M.; Marenich, A. V.; Bloino, J.; Janesko, B. G.; Gomperts, R.; Mennucci, B.; Hratchian, H. P.; Ortiz, J. V.; Izmaylov, A. F.; Sonnenberg, J. L.; Williams-Young, D.; Ding, F.; Lipparini, F.; Egidi, F.; Goings, J.; Peng, B.; Petrone, A.; Henderson, T.; Ranasinghe, D.; Zakrzewski, V. G.; Gao, J.; Rega, N.; Zheng, G.; Liang, W.; Hada, M.; Ehara, M.; Toyota, K.; Fukuda, R.; Hasegawa, J.; Ishida, M.; Nakajima, T.; Honda, Y.; Kitao, O.; Nakai, H.; Vreven, T.; Throssell, K.; Montgomery, J. A., Jr.; Peralta, J. E.; Ogliaro, F.; Bearpark, M. J.; Heyd, J. J.; Brothers, E. N.; Kudin, K. N.; Staroverov, V. N.; Keith, T. A.; Kobayashi, R.; Normand, J.; Raghavachari, K.; Rendell, A. P.; Burant, J. C.; Iyengar, S. S.; Tomasi, J.; Cossi, M.; Millam, J. M.; Klene, M.; Adamo, C.; Cammi, R.; Ochterski, J. W.; Martin, R. L.; Morokuma, K.; Farkas, O.; Foresman, J. B.; Fox, D. J. Gaussian, Inc., Wallingford CT, 2016.

(74) Fernández-Alvarez, V. M.; Nappi, M.; Melchiorre, P.; Maseras, F. Computational Study with DFT and Kinetic Models on the Mechanism of

Photoinitiated Aromatic Perfluoroalkylations. *Org. Lett.* **2015**, *17*, 2676–2679.

(75) Willcox, D.; Nouch, R.; Kingsbury, A.; Robinson, D.; Carey, J. V.; Brough, S.; Woodward, S. Kinetic Analysis of Copper(I)/Feringa-Phosphoramidite Catalyzed $AlEt_3$ 1,4-Addition to Cyclohex-2-en-1-one. *ACS Catal.* **2017**, *7*, 6901–6908.

(76) Zhang, T.; Solé-Daura, A.; Fouilloux, H.; Poblet, J. M.; Proust, A.; Carbó, J. J.; Guillemot, G. Reaction Pathway Discrimination in Alkene Oxidation Reactions by Designed Ti-Siloxy-Polyoxometalates. *ChemCatChem* **2021**, *13*, 1220–1229.

(77) Hay, P. J.; Wadt, W. R. Ab Initio Effective Core Potentials for Molecular Calculations. Potentials for the Transition Metal Atoms Sc to Hg. *J. Chem. Phys.* **1985**, *82*, 270–283.

(78) Ehlers, A. W.; Böhme, M.; Dapprich, S.; Gobbi, A.; Höllwarth, A.; Jonas, V.; Köhler, K. F.; Stegmann, R.; Veldkamp, A.; Frenking, G. A Set of F-Polarization Functions for Pseudo-Potential Basis Sets of the Transition Metals Sc-Cu, Y-Ag and La-Au. *Chem. Phys. Lett.* **1993**, *208*, 111–114.

(79) Francl, M. M.; Pietro, W. J.; Hehre, W. J.; Binkley, J. S.; Gordon, M. S.; DeFrees, D. J.; Pople, J. A. Self-consistent Molecular Orbital Methods. XXIII. A Polarization-type Basis Set for Second-row Elements. *J. Chem. Phys.* **1982**, *77*, 3654–3665.

(80) Hariharan, P. C.; Pople, J. A. The Influence of Polarization Functions on Molecular Orbital Hydrogenation Energies. *Theor. Chim. Acta* **1973**, *28*, 213–222.

(81) Hehre, W. J.; Ditchfield, R.; Pople, J. A. Self-Consistent Molecular Orbital Methods. XII. Further Extensions of Gaussian-Type Basis Sets for Use in Molecular Orbital Studies of Organic Molecules. *J. Chem. Phys.* **1972**, *56*, 2257–2261.

(82) Cancès, E.; Mennucci, B.; Tomasi, J. A New Integral Equation Formalism for the Polarizable Continuum Model: Theoretical Background and Applications to Isotropic and Anisotropic Dielectrics. *J. Chem. Phys.* **1997**, *107*, 3032–3041.

(83) Álvarez-Moreno, M.; de Graaf, C.; López, N.; Maseras, F.; Poblet, J. M.; Bo, C. Managing the computational chemistry big data problem: the ioChem-BD platform. *J. Chem. Inf. Model.* **2015**, *55*, 95–103.

(84) Braun, W.; Herron, J. T.; Kahaner, D. K. Acuchem: A computer program for modeling complex chemical reaction systems. *Int. J. Chem. Kinet.* **1988**, *20*, 51–62.

(85) Marcus, R. A.; Sutin, N. Electron transfers in chemistry and biology. *Biochim. Biophys. Acta, Rev. Bioenerg.* **1985**, *811*, 265-322.

(86) Marcus, R. A. Electron transfer reactions in chemistry: theory and experiment (Nobel lecture). *Angew. Chem., Int. Ed. Engl.* **1993**, *32*, 1111-1121.

(87) Vaissier, V.; Barnes, P.; Kirkpatrick, J.; Nelson, J. Influence of polar medium on the reorganization energy of charge transfer between dyes in a dye sensitized film. *Phys. Chem. Chem. Phys.* **2013**, *15*, 4804-4814.

(88) Marinho, S. M.; Ha-Thi, M.-H.; Pham, V.-T.; Quaranta, A.; Pino, T.; Lefumeux, C.; Chamaillé, T.; Leibl, W.; Aukauloo, A. Time-Resolved Interception of Multiple-Charge Accumulation in a Sensitizer–Acceptor Dyad. *Angew. Chem. Int. Ed.* **2017**, *56*, 15936-15940.

Table of Contents artwork

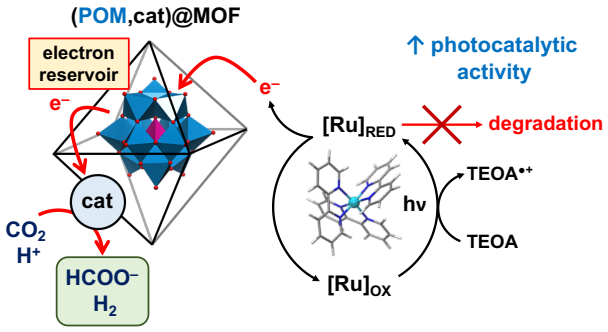

Insert Table of Contents artwork here